Int. J. Multiphase Flow. Vol. 2. pp. 51–66. Pergamon/Elsevier. 1975. Printed in Great Britain.

HORIZONTAL BUBBLE FLOW

T. L. HOLMES* and T. W. F. RUSSELL

Department of Chemical Engineering, University of Delaware, Newark, Delaware 19711, U.S.A.

(*Received* 10 *April* 1974)

Abstract—An experimental investigation of cocurrent bubble flow in 0.0254 m and 0.0508 m diameter horizontal pipelines has been performed. Gas and liquid mass velocities ranged from 0.00955 to 0.675 and 2720 to 6040 kg/m^2 sec, respectively, and gas-phase holdups or void fractions ranged from 0.13 to 7.59%.

High speed motion pictures revealed that the gas, introduced into the liquid with a concentric nozzle, emerged in the form of a rough jet which was ultimately sheared into 1×10^{-3} to 3×10^{-3} m diameter bubbles. Approximately 4 meters downstream from the nozzle, a well developed bubble flow was observed where bubble number density and axial velocity were constant with respect to axial position in the pipeline. Bubble velocities ranged from 0.001 to 0.57 m/sec greater than the average liquid velocities. Bubble radial and circumferential spatial distributions were found to be a strong function of the degree of turbulence in the liquid phase. Because of these turbulent flow conditions, bubble shapes were much different than those of equivalent diameter bubbles rising in stagnant liquids. A sphere-ellipsoid of revolution model was developed for characterization of bubble shape and computation of gas–liquid interfacial area and two-phase pressure drop.

INTRODUCTION

The need for direct contact of a gas phase with a continuous liquid phase for purposes of heat and mass transfer between phases and/or subsequent chemical reaction in the liquid phase is frequently met in the chemical process industries. In general, the efficiency of the two-phase contactors used is a function of how the phases are mixed and how the resulting dispersion is dynamically maintained in the process equipment. Two system geometries which provide limits on processing performance are the tank-type and tubular contactors. In both system geometries, the dispersion results from injecting the gas into the liquid phase. The maintenance of the dispersion is achieved by creating significant shear forces in the liquid phase, either with an impeller in the tank-type system or by the wall shear in the tubular system.

High interfacial areas can be realized in a horizontal pipeline contactor if pipe size, fluid physical properties, and mass flow rates of each phase are selected so that a fine-grained, gas-in-liquid dispersion results. The characterization of the dispersions found in cocurrent gas–liquid flow in horizontal pipelines is thus a necessary first step in solving the general problems of heat, mass, and momentum transfer.

In this work we consider the basic fluid mechanics of horizontal bubble flow in order to provide a foundation for study of the more general design problem.

EXPERIMENTAL EQUIPMENT AND PROCEDURE

The experimental apparatus consisted of horizontal 0.0254 and 0.0508 m i.d. polymethylmethacrylate (PMMA) piping systems plus a high speed movie camera. Air was introduced cocurrently into a highly turbulent water stream *via* a nozzle centred in the PMMA pipeline. The nozzles were constructed of stainless steel tubing, with inside diameters of 0.003 and 0.00431 m for the 0.0254 and 0.0508 m i.d. pipeline systems, respectively. For both systems, the nozzles extended into the pipelines for 1.88 m. This provided

* Present address: Engineering Service Division, E. I. du Pont de Nemours and Company, Wilmington, Delaware.

a 1.88 m entrance section for the liquid flow to become steady. The test section for taking pictures was 5.49 m long and exit sections of 2.35 and 3.3 m for the 0.0254 and 0.0508 m i.d. pipelines were provided, respectively. Pressure taps were installed on each pipeline for measurement of static pressure and two-phase pressure drop. After passing through the two-phase pipeline the air was vented to the atmosphere.

The water system formed a closed loop. Tap water was used to fill a feed tank. From this tank the water was pumped through an orifice into the two-phase pipeline. After passing through the two-phase section the water was recycled to the feed tank. Additional details of the experimental apparatus are given by Holmes (1973).

The photographic equipment consisted of a 16 mm rapid start movie camera, fabricated by L. C. Eichner of Clifton, New Jersey; an Edgerton Type 501 high speed strobe; and a synchronization unit. The camera was shutterless and the high frequency strobe served as a means of forming each photograph or frame. In operation, light from a strobe flash passed through the PMMA pipeline, into the camera lens and onto the film moving by the lens. Linear film speed was varied by adjusting the speed of the rotating film drive rolls. Once the desired film speed was selected, the strobe was triggered by a signal generated by the passage of light through the standard sprocket holes in the film, thus producing one picture for each hole. With an FX2 xenon filled spark tube and a 0.01 μF discharge capacitor, flash durations of 1.2 μ sec were obtained.

The speed at which the 16 mm film passed by the camera lens was determined with the aid of a General Radio Type 1531 AB Strobotac. This strobe was set on 3600 flashes/min and pointed directly into the camera lens. Several photographs were then taken. With a knowledge of the distance between flash marks on the developed film and the strobe frequency the linear film speed was calculated to be 9.61 m/sec or 1260 frames/sec. This film speed was used in all subsequent photographic work.

To eliminate distortion special water filled view boxes were constructed for each pipeline. The effectiveness of the view boxes in reducing distortion was determined by photographing 3.96×10^{-3} m and 11.90×10^{-3} m steel spheres located at various points inside the water filled pipelines. The maximum distortion found for the 0.0254 m i.d. pipeline system was 4.7% in the vertical dimension, while the maximum found for the 0.0508 m system was 12.1% in the vertical dimension. As discussed by Cichy (1971), distortion as great as 155% is not uncommon when objects are photographed in a 0.0254 m diameter pipe without a view box.

Calibration of the water metering system was achieved by measuring both the pressure drop across the orifice and the mass flow rate of water into the open air feed tank. Since the flow through the orifice was always turbulent for the liquid rates of interest, the familiar orifice equation provided a convenient means of checking the consistency of measured mass flow rates and pressure drops.

The rotameters for gas metering were calibrated with a wet test meter and by a volumetric water displacement technique. Reasonable correspondence was found. As a third check, comparison with the standard Matheson rotameter calibration graphs was performed. Excellent agreement was observed.

Two-phase pressure drop was determined by measuring the liquid-phase pressure drop over various segments of the test section. Mercury manometer systems, with water filled tubing lines from the pressure taps to the manometers, were used for this purpose.

In performing the runs for data acquisition, the air and water rates were set at the desired values and heat from the pump was used to bring the water temperature to 293°K. A small excess water stream was turned on and some heat was removed by withdrawing a small side stream from the system to maintain the system temperatures and the liquid level in the open air tank constant.

After reaching steady state, photographs were taken at various points ranging from 0.92

to 5.49 m downstream from the nozzle. For each exposure, film was allowed to pass by the camera lens for approximately 1/7 sec. This procedure resulted in a sequence of approximately 160 frames, hereafter called a shot. To check the reproducibility of the photographic data at least two shots were taken at each point of interest along a pipeline.

To ensure that the depth of field of the movie camera was sufficient to capture all of the bubbles in the dimension perpendicular to the flow, a special grid was placed on the back of the view box. Before taking pictures the camera focus was adjusted until both the grid and a reference object on the front of the view box could be seen clearly. In addition to providing a necessary depth of field check, the grid provided a useful reference length dimension on each photograph. These grids were constructed so that linear grid spacings of 4×10^{-3} and 8×10^{-3} m could be seen for the 0.0254 and 0.0508 m i.d. pipeline systems, respectively.

EXPERIMENTAL RESULTS

The flow conditions investigated are summarized in table 1. Gas mass velocities (G^* values) of 0.675, 0.0955 and 0.00955 kg/m^2 sec were used with average axial liquid velocities from 2.73 to 6.1 m/sec. The corresponding liquid-phase Reynolds numbers ranged from approximately 90,000 to 180,000. Also shown in this table are measured mass flow rate, W, and two-phase pressure drop, $(\Delta P/L)_{TP}$, data. The flow conditions of interest are plotted on a modified Baker chart in figure 1. Data for the stratified-plug and plug-bubble transitions at the lower gas rates, established by Cichy (1971), were used in the construction of this figure.

For each of the photographic locations considered here, at least two shots were taken, resulting in approximately 10,000 photographs of the bubble flows of interest. For brevity, only a single typical photograph is shown here.

The effect of a turbulently flowing liquid upon bubble size is illustrated in figure 2. For this run, the gas emerges from the nozzle in the form of a rough jet. Once leaving the nozzle, relatively large bubbles are formed as can be seen from the photograph taken 0.92 m downstream. These large bubbles are then sheared into smaller ones as they flow downstream. At a distance sufficiently far from the nozzle an equilibrium bubble size is achieved. When this configuration is attained, the number of bubbles per unit volume of pipeline is constant with respect to axial position. For the fluid flow rates investigated this condition was

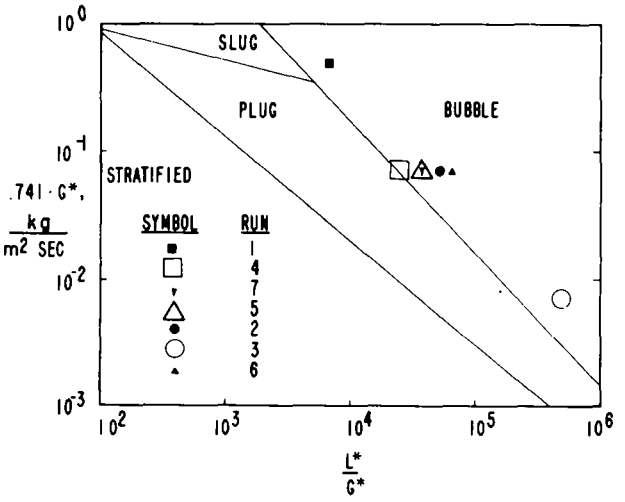

Figure 1. Extended Baker chart.

Table 1. Flow conditions investigated

Run number	Pipe i.d. (m)	Liquid flow rate W_L (kg/sec)	Liquid flow rate $L^* \times 10^{-3}$ (kg/m² sec)	Gas flow rate $W_G \times 10^8$ (kg/sec)	Gas flow rate $G^* \times 10^3$ (kg/m² sec)	$(L^*/G^*) \times 10^{-3}$	Air temp. (°K)	Water temp. (°K)	$\left(\frac{\Delta P}{L}\right)_{TP} \times 10^{-3}$ (N/m³)
1	0.0254	2.32	4.55	343.00	675.00	6.75	295	293	7.49
2	0.0254	2.33	4.59	48.50	95.50	48.10	296	293	7.69
3	0.0254	2.35	4.61	4.85	9.55	484.00	296	293	7.61
4	0.0508	5.55	2.72	194.00	95.50	28.60	296	293	1.34
5	0.0508	7.12	3.50	194.00	95.50	36.70	295	293	2.05
6	0.0254	3.07	6.04	48.50	95.50	63.30	296	293	15.70
7	0.0254	1.75	3.44	48.50	95.50	36.10	296	293	4.25

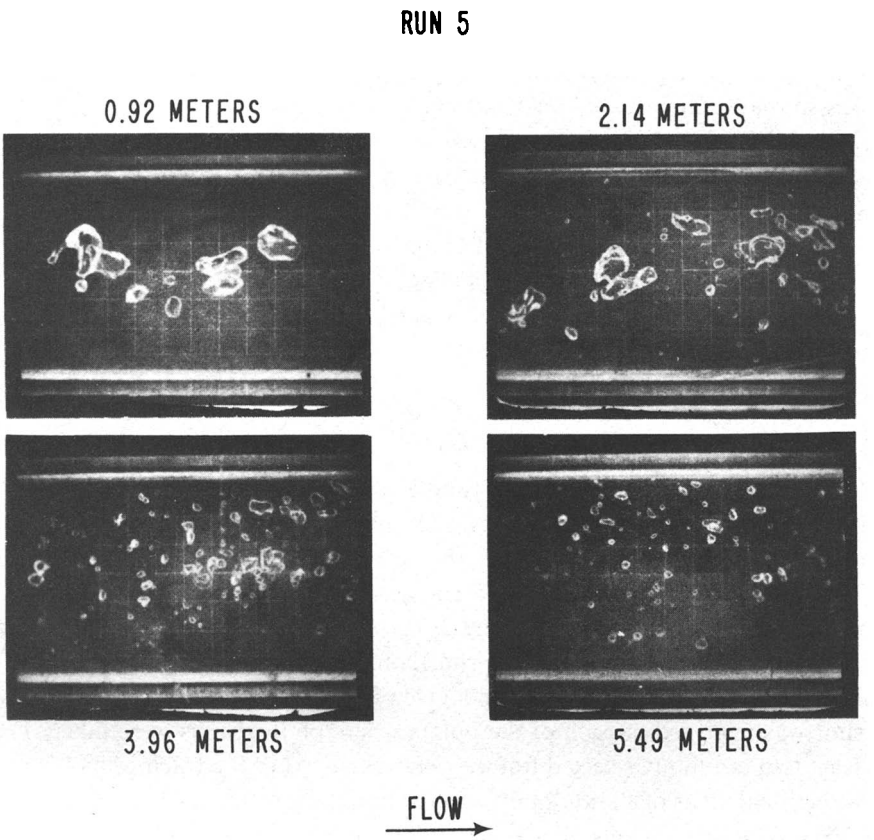

Figure 2. Typical bubble size distributions as a function of distance downstream from nozzle.

reached in approximately 3.7 m in the 0.0254 m i.d. pipeline and in approximately 4.6 m in the 0.508 m diameter pipeline (figure 4).

A wide variety of bubble *in situ* configurations are possible depending upon liquid and gas mass velocities, fluid physical properties, and pipe size. The photographic data necessary to characterize these takes the form of number density, bubble size, and bubble velocity data. These results were obtained by projecting the developed film from 2 to 7 times actual size and taking appropriate measurements.

A Bell and Howell, Type BD, 16 mm motion picture projector was used to project each frame of interest onto a special form. A typical set of results is shown in figure 3. Projected

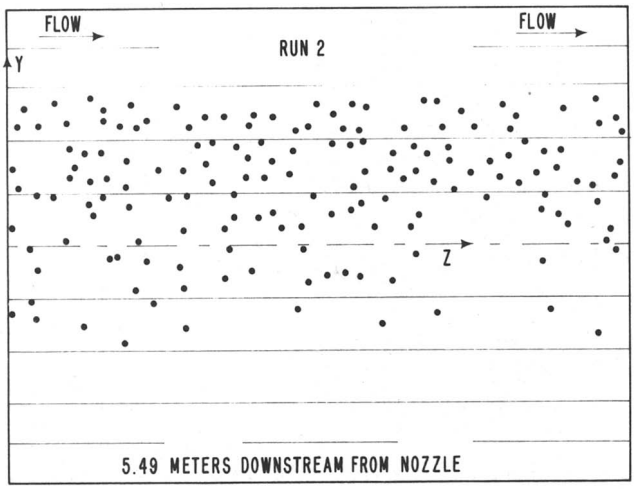

Figure 3. Bubble number density data.

images are four times actual size for the 0.0254 m i.d. pipeline runs and twice actual size for those in the 0.0508 m pipeline. The inside pipe diameter in figure 3 has been divided into six regions so that bubble spatial distributions may be obtained.

Such bubble number data were obtained at each of the locations where photographs were taken for runs 2–7. The bubbles on at least five frames were counted for any given shot and arithmetic mean values were used to characterize the average bubble number density at each location. Two types of average bubble number density data were obtained: the number of bubbles per unit volume of pipeline, N_B, and the number of bubbles per unit volume of pipeline for each of the 6-pipe slices, N_{Bi}. These variables are related by the following equation:

$$N_B = \sum_{i=1}^{6} N_{Bi} V_i / V_T. \qquad [1]$$

Plots of N_B and N_{Bi} may be seen in figures 4 and 5, respectively. A summary of experimentally determined bubble number density values is in table 2.

To determine bubble size distributions, the developed films were projected onto a form similar in appearance to that in figure 3. The actual appearance of the projected bubble images was similar to those shown in figure 2. The circumference of each bubble on a given frame was then traced onto the form. For run 1, only the bubbles below the centerline were traced. For the other runs, all bubbles on a given frame were traced.

One shot was analyzed at each of the points where photographs were taken. For each shot at least two randomly selected frames were traced. After the tracings had been made, the cross-sectional areas of 80 randomly selected bubbles per tracing were measured with a K & E Type 4236M compensating polar planimeter. For any given bubble, the cross-sectional area so determined was that which was in a plane parallel with the pipe centerline.

Bubble cross-sectional area distributions were found to range from approximately normal for the highest shear-rate runs to approximately log-normal for those in the 0.0508 m diameter pipeline (see table 1 for the flow conditions investigated). Arithmetic mean cross-sectional area values (A values), used here to characterize average bubble size, are presented in table 3.

To determine bubble velocity distributions, the 16 mm photographs were projected onto a 0.28 m × 0.431 m form similar in appearance to that shown in figure 6. Projected images were seven times actual size for the 0.0254 m diameter pipeline runs and four times actual size for those in the 0.0508 m diameter pipeline. A bubble was selected and traced onto the form. The next frame was then projected and the same bubble again traced onto the form.

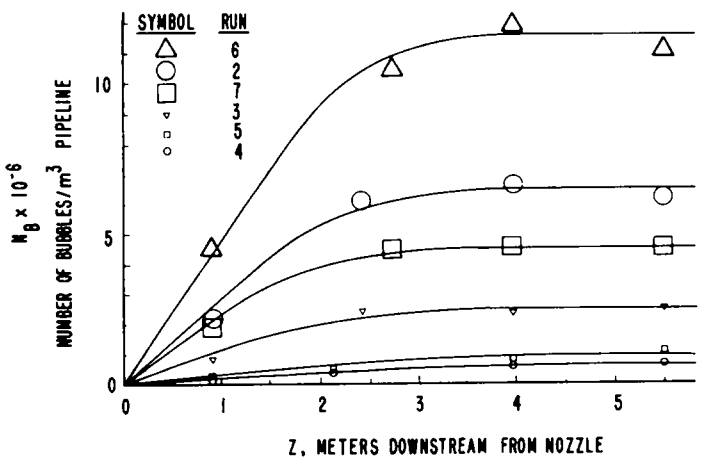

Figure 4. Results of bubble count.

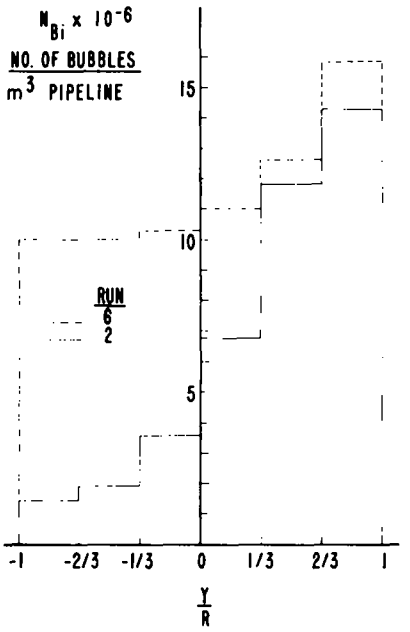

Figure 5. Bubble number density distributions.

This process was repeated until the bubble was either lost in a sea of bubbles or traveled off the form.

Once a tracing was completed, velocity component data were obtained by the following step-by-step method. (1) Since the linear film speed was measured and found to be 1259 frames/sec, the time increment to be used in calculating bubble velocities is 0.0007943 sec. (2) Both vertical (Y) and axial (Z) coordinates were recorded for each bubble.

Table 2. Average bubble number density, 5.49 m downstream from nozzle

Run number (see table 1)	Shot number	$N_B \times 10^{-6}$ Number of bubbles / m^3 of pipeline
2	1	6.231
3	5	2.538
4	9	0.676
5	9	1.044
6	8	11.269
7	9	4.500

Table 3. Average bubble cross-sectional area, 5.49 m downstream from nozzle

Run number	Shot number	$A \times 10^4$ (m^2)
1	1	1.209
2	1	1.035
3	4	0.937
4	8	5.382
5	8	4.464
6	8	0.606
7	8	1.849

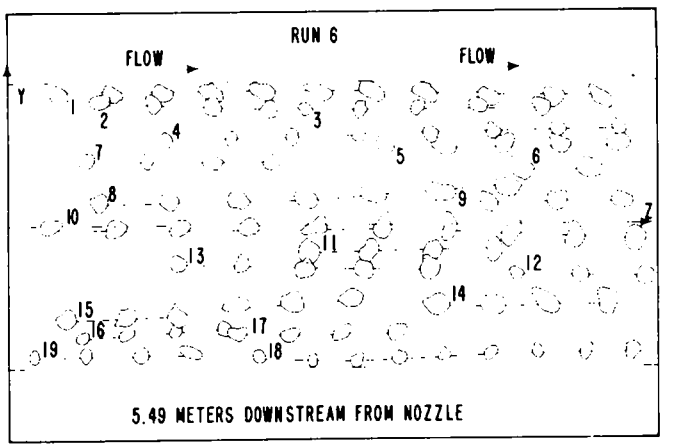

Figure 6. Typical bubble velocity tracing.

The Y coordinate was chosen to be the perpendicular distance from the pipe centerline to the edge of the bubble closest to the centerline. The Z coordinate, in turn, was chosen to be the perpendicular distance from a Y axis to the edge of the bubble closest to the Y axis (figure 6). If a bubble crossed the pipe centerline in its travel, the initial convention for determining the Y coordinate was retained. (3) After the coordinates were recorded for a given bubble trajectory of say, n consecutive frames, $n - 1$, Z and $n - 1$, Y velocity components could be calculated.

The velocity of a bubble in a turbulently flowing liquid is dependent upon its position in the pipeline and upon its size. To include both of these effects in the analysis, large and small bubbles at many different positions in the pipe cross section were included in the tracings.

To quantitatively characterize average bubble velocity, mean values were used. Some typical velocity distributions are presented in figures 7 and 8. The mean Z, $\bar{v}_{BZ}$, and Y, $\bar{v}_{BY}$, velocity components are shown as dotted lines on these figures. As expected, the average Y velocity component is practically zero since there is no net flow in this direction. The maximum Y component velocity observed is approximately 14% of the average axial velocity.

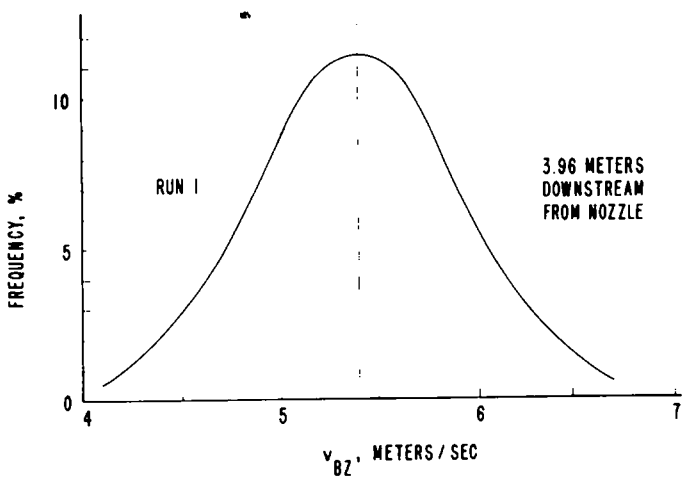

Figure 7. Bubble axial velocity distribution.

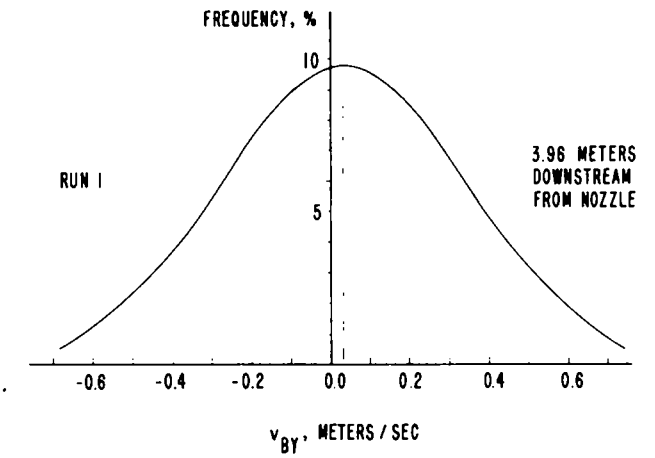

Figure 8. Bubble vertical velocity distribution.

Additional bubble velocity data may be seen in table 4. Upstream values are included for run 1 to show that once a terminal axial velocity is attained, it remains fairly constant with respect to axial position in the pipeline. As can be seen from this table, this terminal bubble velocity is reached by the time the two-phase mixture passes the 0.92 m downstream from nozzle location.

ANALYSIS OF RESULTS

With the experimental data obtained, two important quantities necessary for the design of pipeline contactors may be calculated: (1) interfacial area and (2) pressure drop. To compute interfacial area, average bubble velocities are used to obtain gas-phase holdup values. Bubble number density data and this holdup information are then combined to determine a shape factor for each run. The bubble photographic data and cross-sectional area data are then analyzed and a means of computing interfacial area is outlined. The bubble shape is also incorporated into a drag correlation to predict two-phase pressure drop.

(1) *Interfacial area*

The dispersed phase holdup, R_G, may be calculated from the following gas-phase material balance, which is discussed by Cichy *et al.* (1969):

$$R_G = W_G/\rho_G \bar{v}_{BZ} A_c. \qquad [2]$$

Table 4. Average bubble axial velocity

Run number	Shot number	Number of Z velocity components considered	Distance downstream from nozzle (m)	$\bar{v}_{BZ}$ (m/sec)
1	3	54	0.92	5.42
1	4	67	3.96	5.40
1	1	100	5.49	5.36
2	1	123	5.49	4.84
3	5	132	5.49	4.66
4	9	167	5.49	2.87
5	9	243	5.49	4.09
6	8	83	5.49	6.67
7	9	133	5.49	3.59

Table 5. Calculated dispersed-phase holdup and slip velocity

Run number	R_G Experimental[2]	R_G Hughmark correlation	% Deviation of Hughmark from experimental R_G value	U (m/sec) [3]
1	0.07950	0.06506	- 18.16	0.40900
2	0.01210	0.00997	- 17.60	0.16480
3	0.00126	0.00101	- 20.63	0.00122
4	0.00687	0.00559	- 18.63	0.10680
5	0.00487	0.00447	- 8.21	0.57100
6	0.00839	0.00732	- 12.75	0.54900
7	0.01654	0.01321	- 20.13	0.06710

The density of air, ρ_G, is obtained by using the ideal gas law. The pertinent W_G, gas flow rate, and $\bar{v}_{BZ}$ data are in tables 1 and 4, respectively, and A_c is the cross-sectional area of the pipeline. Once R_G is known, the slip velocity, U, may be calculated from the following equation, which is discussed in more detail by Nicklin (1962):

$$U = \bar{v}_{BZ} - \frac{W_L}{\rho_L(1 - R_G)A_c} \quad [3]$$

where ρ_L and W_L are the density and flow rate of the liquid, respectively. Results determined with [2] and [3] are in table 5. The R_G values calculated with correlation of Hughmark (1962), also shown here, are in reasonable agreement with those calculated from experimental data.

Once the dispersed phase holdup is known, the average bubble volume for each of these runs may be calculated from the following equation

$$\bar{V}_{DG} = \frac{R_G}{N_B}. \quad [4]$$

The average bubble number density data required are in table 2. After $\bar{V}_{DG}$ is known, the shape factor α may be calculated as follows

$$A = \alpha \bar{V}_{DG}^{2/3}, \quad [5]$$

where A is the cross-sectional area of an average bubble in a plane parallel with the flow. These area data are the planimeter values listed in table 3. Results determined from [4] and [5] are in table 6. No results are shown for run 1 because reliable number density data were not obtained.

The simplest model for characterization of bubble size is an average spherically equivalent diameter. Since the shape is far from spherical in the horizontal bubble flows observed in this study, this diameter does not accurately represent the physical situation. A slightly more complex, two parameter model is proposed in which the downstream portion of the bubble is assumed to be a hemisphere and the upstream portion is assumed to be one-half of

Table 6. Average bubble volumes and shape factors

Run number	$V_{DG} \times 10^9$ (m^3)	α
2	1.940	0.6650
3	0.496	1.5391
4	10.160	1.1629
5	4.680	1.5928
6	0.744	0.7378
7	3.680	0.7758

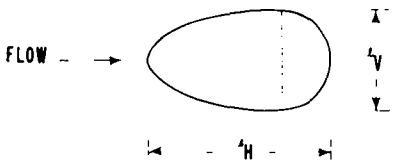

Figure 9. Proposed bubble shape model.

an ellipsoid of revolution. This characterization of the shape may be seen in figure 9. Depending upon the relative lengths of l_V and l_H, a number of shapes are possible. When l_V equals l_H the bubbles are spherical. If l_H is greater than l_V, the upstream portion of the bubble is a prolate ellipsoid and if l_H is less than l_V this portion is an oblate ellipsoid. For the latter case, if l_H is less than $1/2\, l_V$, the back of the bubble is caved in and the resulting shape resembles that of the mushroom-like spherical cap bubbles. The prolate and oblate shapes resemble those discussed by Hinze (1955) for cigar-shaped and lenticular deformation, respectively.

The cross-sectional area of the proposed bubble in a plane parallel with the flow, A, the volume, V_{DG}, and the surface area, S, may be written in terms of l_V and l_H as follows:

$$A = \frac{\pi}{4}(l_V l_H) \qquad [6]$$

and

$$V_{DG} = \frac{\pi}{6} l_V^2 l_H. \qquad [7]$$

For $l_H > l_V$,

$$S = \frac{\pi l_V}{4}\left[3l_V + \frac{2(l_H - l_V/2)^2}{[l_H(l_H - l_V)]^{1/2}} \sin^{-1}\left(\frac{[l_H(l_H - l_V)]^{1/2}}{(l_H - l_V/2)}\right)\right]. \qquad [8]$$

For $l_H < l_V$,

$$S = \frac{\pi l_V}{4}\left[3l_V + \frac{2(l_H - l_V/2)^2}{[l_H(l_V - l_H)]^{1/2}} \ln\left(\frac{2[(l_H(l_V - l_H)]^{1/2} + l_V}{2l_H - l_V}\right)\right]. \qquad [9]$$

Substituting [6] for bubble cross-sectional area and the equation for bubble volume [7] into [5], yields

$$\alpha = 1.209\left(\frac{l_H}{l_V}\right)^{1/3}. \qquad [10]$$

For a sphere, $l_V = l_H$, and $\alpha = 1.209$. The shape factors calculated from [5] for other familiar shapes are: cube, $\alpha = 1.0$; rectangle formed by adding two cubes together, $\alpha = 1.26$. From the data in table 6, it can be seen that the shapes of the bubbles of interest are not spherical.

Table 7. Average bubble size data

Run number	Sphere-Ellipsoid of Revolution Model			Sphere Model
	$l_H \times 10^3$ (m)	$l_V \times 10^3$ (m)	$d_{GM} \times 10^3$ (m)	$d_e = \left(\frac{6}{\pi} V_{DG}\right)^{1/3} \times 10^{-3}$ (m)
2	0.468	2.812	1.147	1.548
3	1.503	0.794	1.091	0.982
4	2.520	2.832	2.671	2.687
5	3.615	1.572	2.384	2.075
6	0.419	1.844	0.879	1.124
7	0.789	2.986	1.535	1.916

Since A and α are known, [6] and [10] may be solved for the characteristic length parameters, l_V and l_H, in the sphere-ellipsoid of revolution model. Results of this calculation are in table 7. The geometric mean bubble diameter d_{GM}, defined as $(l_V l_H)^{1/2}$, and a spherically equivalent diameter, d_e, calculated from the $\overline{V}_{DG}$ data in table 6 are also included.

The average bubble diameters calculated from the two models discussed above are approximately the same. The more complicated sphere-ellipsoid model is needed if the interfacial area is to be correctly computed. Bubble surface areas calculated with the sphere model may be as little as one half those calculated with the sphere–ellipsoid model so corresponding interfacial area values may be low by the same factor (see table 8).

The bubble length parameters l_H and l_V in table 7 may be used along with the standard equations for an ellipse and a circle to calculate the bubble shapes of interest:

$$\text{Ellipse:} \quad \frac{Z^2}{(l_H - l_V/2)^2} + \frac{Y^2}{(l_V/2)^2} = 1 \qquad [11]$$

$$\text{Circle:} \quad Z^2 + Y^2 = (l_V/2)^2. \qquad [12]$$

where Z is the axis parallel with the flow. Results of these calculations are shown in figure 10. The view shown here is the side view one would see by looking through the pipe wall. Both oblate and prolate ellipsoid of revolution shapes for the upstream portion of bubbles are observed. Note that for run 2, the upstream portion is caved in. Similar results were also observed for runs 6 and 7 (not shown). For these runs, the dispersed phase holdups are greater than those for the runs where the backs are not caved in. This shape might possibly be the result of bubble collisions. The bubbles shown in figure 10 should be compared with the bubble photographs in figure 2, keeping in mind that average sizes and shapes are of interest here.

Using the characteristic bubble length dimensions l_V and l_H developed for the sphere–ellipsoid model and listed in table 7, the average bubble surface area, S, may be calculated from [8] and [9]. These values, then plus the average bubble number density data in table 2, provide the basic input data for determining the average interfacial area, a. Results of these calculations, $a = N_B S$, are in table 8. For comparison purposes, interfacial area values calculated with the sphere model are also shown. These were estimated with the same N_B data, but with an average surface area calculated from the d_e values in table 7.

(2) *Pressure drop*

The two-phase pressure drop may be predicted by the following equation

$$\left(\frac{\Delta P}{L}\right)_{TP} = \frac{4}{D}\frac{\rho_L v_{LS}^2}{2} f + \frac{3R_G}{2l_V}\frac{\rho_L U^2}{2} C_D, \qquad [13]$$

where D is the inside diameter of the pipeline and v_{LS} is the superficial liquid-phase velocity.

Table 8. Average bubble suface and interfacial areas

Run number	Sphere-ellipsoid of revolution model: Bubble surface area, Equation number	Bubble surface area, $S \times 10^5$ (m^2)	Interfacial area, $a \times 10^{-2}$ (m^2/m^3)	Sphere model: $a = \pi d_e^2 N_B \times 10^2$ (m^2/m^3)
2	9	2.220	1.3830	0.4690
3	8	0.326	0.0829	0.0769
4	9	2.339	0.1581	0.1533
5	8	1.517	0.1578	0.1407
6	9	0.916	1.0328	0.4473
7	9	2.345	1.0553	0.5190

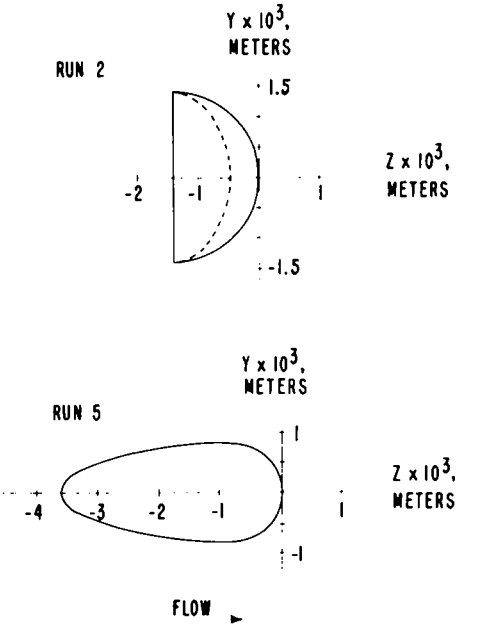

Figure 10. Average bubble sizes calculated from experimental data. Sphere-ellipsoid of revolution model -side view.

Here, the pressure drop is assumed to be the sum of that due to the liquid flowing alone and an excess pressure drop. This assumption has been verified experimentally by Hockmuth & Sutera (1970) for the flow of large spherical cap bubbles in horizontal, low Reynolds number tube flow. Use of [13] for the turbulent liquid case of interest is justified on the basis that excellent agreement with experimental data is observed.

Using the characteristic bubble length dimension perpendicular to the flow, l_V, and the average relative velocity values in table 5, the bubble Reynolds number may be calculated from the following equation discussed by Gorring & Katz (1962):

$$(\mathrm{Re})_b = \frac{l_V U \rho_L}{\mu_L} \qquad [14]$$

where μ_L is the liquid viscosity.

Once these values are known, the appropriate drag coefficients to be used in [13] may be obtained from the experimental data of Haberman & Morton (1953) for air bubbles rising in stagnant tap water. With the liquid mass flow rate data in table 1, the Fanning friction factor required was calculated from [15], which is discussed in more detail by McCabe & Smith (1956):

$$f = 0.0014 + \frac{0.125}{(\mathrm{Re})_L^{0.32}}. \qquad [15]$$

Results of these calculations are in table 9.

Table 9. Drag coefficients and friction factors

Run number	Bubble drag coefficients $(\mathrm{Re})_b$	C_D	Liquid-phase friction factors $(\mathrm{Re})_L$	f
2	496.77	0.6613	119,000	0.00437
3	5.39	6.8018	119,700	0.00436
4	323.18	0.6066	141,500	0.00421
5	930.03	1.0407	181,300	0.00399
6	998.72	1.1381	156,500	0.00412
7	163.41	0.7480	89,300	0.00466

Table 10. Comparison of experimental and predicted two-phase pressure drop

Run number	Predicted pressure drop $\left(\frac{\Delta P}{L}\right)_L \times 10^{-2}$ (N/m³)	$\left(\frac{\Delta P}{L}\right)_E \times 10^{-2}$ (N/m³)	$\left(\frac{\Delta P}{L}\right)_{TP} \times 10^{-2}$ (N/m³)	Experimental $\left(\frac{\Delta P}{L}\right)_{TP} \times 10^{-2}$ (N/m³)	% Deviation from experimental value
2	72.922	3.864	76.786	76.867	−0.11
3	73.647	0.002	73.649	76.189	−3.33
4	12.414	0.156	12.570	13.430	−0.51
5	19.385	3.553	22.938	20.614	11.26
6	118.964	48.402	167.366	156.673	6.83
7	43.773	0.341	44.114	42.503	3.78

The liquid-phase Reynolds numbers and friction factors shown in this table were determined by assuming that the liquid was flowing alone in the pipeline in accordance with the assumptions involved in the derivation of [13].

With the results shown in table 9, and the dispersed phase holdup data in table 5, the two-phase pressure drop may be predicted. Results are in table 10. For runs 2, 3, 4, 5, and 7 the two-phase pressure drop is approximately equal to that calculated assuming the liquid is flowing alone. The results for run 6, however, show that the excess pressure drop is very significant. Run 6 is the highest liquid shear rate case considered in this study (see table 1), and is the situation more likely to be encountered in practice.

CONCLUSIONS

(1) An experimental investigation of cocurrent gas(air)–water flow has been performed in horizontal 0.0254 m and 0.0508 m i.d. pipeline systems for bubble flow conditions located on the lower right-hand portion of the Baker chart. The gas, introduced into the turbulently flowing liquid through a nozzle, emerged in the form of a rough jet and breakup occurred in transition regions of approximately 3.7 and 4.6 m in length for the 0.0254 and 0.0508 m i.d. pipeline systems, respectively. Immediately downstream from these transition regions, well developed bubble flows, where average bubble number density and velocity were constant with respect to axial position, were found. For the well developed flows, radial bubble distribution was observed to be a strong function of the shear field in the liquid phase with a nearly homogeneous dispersion being formed at the highest liquid flow rates.

(2) Analysis of photographic data of well developed bubble flow indicated that bubble size and velocity distributions may be approximated with the Gaussian distribution. Average bubble diameters ranged from approximately 1×10^{-3} to 3×10^{-3} m for the air–water system and bubble shape was characterized by a sphere–ellipsoid of revolution model. Average axial bubble velocities ranging from 1×10^{-3} to 5.7×10^{-1} m/sec greater than the average liquid velocities were found.

(3) Interfacial areas calculated with the sphere-ellipsoid of revolution model ranged from 8.29 to 138 m^2/m^3 for gas-phase holdups ranging from 0.487 to 1.65%, respectively. Corresponding values calculated with the sphere model are low by a factor of 2, showing that the former model is needed if interfacial area is to be correctly computed.

(4) A method for predicting two-phase pressure drop from that due to the liquid flowing alone and that due to the movement of the bubbles through the liquid has been presented. Reasonable comparison with experimental pressure drop data was found when bubble motion was characterized with drag coefficient data developed for stagnant liquid systems.

REFERENCES

CICHY, P. T. 1971 Formation and Movement of Gas Cavities in Stationary and Flowing Liquids. Ph.D. Thesis, University of Delaware.

CICHY, P. T., ULTMAN, J. S. & RUSSELL, T. W. F. 1969 Two-phase reactor design tubular reactors– Reactor model development. *Ind. Engng Chem.* **61**, 6–14.

GORRING, R. L. & KATZ, D. L. 1962 Bubble rise in a packed bed saturated with liquids. *AIChE J.* **8**, 123–126.

HABERMAN, W. L. & MORTON, R. K. 1953 An Experimental Investigation of the Drag and Shape of Air Bubbles Rising in Various Liquids, The David W. Taylor Model Basin. Report 802, N5715–102, Navy Department.

HINZE, J. O. 1955 Fundamentals of the hydrodynamic mechanism splitting in dispersion processes. *AIChE J.* **1**, 289–295.

HOCKMUTH, R. M. & SUTERA, S. P. 1970 Spherical caps in low Reynolds-number tube flow. *Chem. Engng Sci.* **25**, 593–604.

HOLMES, T. L. 1973 Fluid Mechanics of Horizontal Bubble Flow. Ph.D. Thesis, University of Delaware.

HUGHMARK, G. A. 1962 Holdup in gas–liquid flow. *Chem. Engng Prog.* **58**, 62–65.

MCCABE, W. L. & SMITH, J. C. 1956 *Unit Operations of Chemical Engineering*, p.67. McGraw–Hill, New York.

NICKLIN, D. J. 1962 Two-phase bubble flow. *Chem. Engng Sci.* **17**, 693–702.

Résumé Une étude expérimentale a été menée sur des écoulements cocourants à bulles dans des conduites horizontales de 0.0254 m et de 0.0508 m die diamètre. Les vitesses massiques du gaz et du liquide ont varié respectivement de 0.00955 à 0.675 et de 2720 à 6040 kg/m^2-sec, et la fraction volumique de phase gazeuse a varié de 0.13 à 7.59%.

La cinématographie ultra-rapide montre que le gaz, introduit dans le liquide par un orifice concentrique, émerge sous forme d'un jet grossier qui se résoud finalement en bulles de 1×10^{-3} à 3×10^{-3} m de diamètre. Environ 4 mètres en aval de l'injecteur, on observe un écoulement bien établi de bulles dont le nombre par unité de volume et la vitesse axiale ne dépendent pas de la position axiale dans la conduite. Les vitesses de bulles sont supérieures de 0.001 à 0.57 m/sec aux vitesses moyennes du liquide. Les distributions spatiales radiale et circonférentielle des bulles sont fortement dépendantes du degré de turbulence de la phase liquide. En raison de ces conditions d'écoulement turbulent, les formes des bulles sont très différentes de celles montant, avec des diamètres équivalents, dans des liquides au repos. Un modèle à sphère et ellipsoïde de révolution a été mis au point pour caractériser la forme des bulles, afin de calculer la surface de l'interface gaz liquide ainsi que la chute de pression diphasique.

Auszug—Es wurde eine gleichsinnige Blasenstroemung in wagerechten Rohrleitunge von 25,4 und 50,8 mm Durchmesser experimentell untersucht. Die Massengeschwindigkeiten von Gas und Fluessigkeit legan zwischen 0,00955 und 0,675, und zwischen 2720 und 6040 kg/m^{2}s, respektive, bei einem Gasphasengehalt von 0,13 bis 7,59%. Hochgeschwindigkeits-Filmaufnahmen enthuellten, dass das mittels einer konzentrischen Duese in die Fluessigkeit eingebrachte Gas in der Form eines rauhen Strahles austrat, der schliesslich in Blasen von 1 bis 3 mm Durchmesser aufgeschert wird. Ungefaehr 4 m unterhalb der Duese wurde eine vollentwickelte Blasenstroemung beobachtet, in der die Blasenzahldichte und axiale Geschwindigkeit in Bezug auf die axiale Lage in der Rohrleitung konstant waren. Die Blasengeschwindigkeiten lagen um 0,001 bis 0,57 m/s ueber den Durchschnittsgeschwindigkeiten der Fluessigkeit. Es wurde gefunden, dass die raeumlichen Verteilungen der Blasen in radialer und in Umfangsrichtung stark vom Turbulenzgrad in der fluessigen Phase abhaengen. Wegen dieser turbulenten Stroemungsverhaeltnisse waren die Blasen in ihrer Form sehr verschieden von Blasen mit aequivalenten Durchmessern, die in ruhender Fluessigkeit aufsteigen. Ein Kugel-Rotationsellipsoid-Modell wurde entwickelt, um die Blasenform zu charakterisieren, und die Flaeche der Trennschicht zwischen Gas und Fluessigkeit und den Zweiphasen-Druckabfall zu berechnen.

Резюме—Проведено экспериментальное исследование потока, несущего пузыри в горизонтальном трубопроводе диаметром 0,0254 м и 0,0508 м. Массовые скорости (расходы) газа и жидкости колебались между 0,00955 и 0,675 и между 2720 и 6070 кг/м^2 сек соответственно, а содержание газовой фазы между 0,13 и 7,59%.

Высокоскоростная киносъемка показала, что газ, вводимый в жидкость концентрическим соплом, вытекает струей неопределенной формы, которая в конечном счете разбивается на пузырьки диаметром от $1 \cdot 10^{-3}$ до $3 \cdot 10^{-3}$ м. Хорошо развитое пузырьковое течение наблюдалось приблизительно в 4 метрах после сопла, где численная концентрация пузырьков и осевая их скорость оставались постоянными соответственно их положению относительно оси трубопровода.

Превышение скорости пузырьков над средней скоростью жидкости колебалось от 0,001 до 0,57 м/сек. Было найдено, что радиальное и окружное распределение пузырьков в пространстве является четкой функцией степени турбулизации жидкой фазы. Ввиду такой турбулентности потока форма пузырьков сильно отличалась от таковой для пузырьков эквивалентного диаметра, подымающихся в стоячей жидкости. Для характеризации формы пузырька и расчета площади поверхности, разделяющей газ и жидкость и понижения двуфазного давления была развита модель эллипсоида вращения.